

Supporting Information

Chemical Vapor Deposition-Prepared Sub-Nanometer Zr Clusters on Pd Surfaces: Promotion of Methane Dry Reforming

Lukas Mayr,^{1,2} Xue-Rong Shi,¹ Norbert Köpfle,¹ Cory A. Milligan,^{2,3} Dmitry Y.
Zemlyanov,² Axel Knop-Gericke,⁴ Michael Hävecker,⁴ Bernhard Klötzer,¹ and Simon
Penner^{1*}

¹ *Institute of Physical Chemistry, University of Innsbruck, Innrain 80-82, Innsbruck, Austria*

² *Birck Nanotechnology Center, Purdue University, 1205 West State Street, West Lafayette,
IN 47907, United States*

³ *School of Chemical Engineering, Purdue University, West Lafayette, Indiana, 47907, United
States*

⁴ *Department of Inorganic Chemistry, Fritz-Haber-Institute of the Max-Planck-Society, Faradayweg
4-6, D-14195 Berlin, Germany*

Keywords: Zirconium-t-butoxide, Palladium, HREELS, Density functional theory, Zr
reduction, Methane Dry Reforming, Methanol Steam Reforming

A XPS Overlayer model

- Coverage estimation by an non-attenuated overlayer model:

$$Coverage \equiv \frac{s_l}{s_s} = \frac{N_l(\theta) \times \Omega_s(E_s) \times A_s(E_s) \times \frac{d\sigma_s}{d\Omega} \times \Lambda_e^{subst}(E_s) \times \cos\theta}{N_s(\theta) \times \Omega_l(E_l) \times A_l(E_l) \times \frac{d\sigma_l}{d\Omega} \times d_s}$$

- Overlayer thickness estimation by an attenuated model:

$$\frac{N_l(\theta)}{N_s(\theta)} = \frac{I_l \times \rho_l \times \frac{d\sigma_l}{d\Omega} \times \Lambda_l(E_l) \times \cos\theta}{I_s \times \rho_s \times \frac{d\sigma_s}{d\Omega} \times \Lambda_s(E_s) \times \cos\theta} \times \frac{\left(1 - \exp\left(\frac{-t}{\Lambda_l(E_l) \times \cos\theta}\right)\right)}{\left(\exp\left(\frac{-t}{\Lambda_l(E_s) \times \cos\theta}\right)\right)}$$

ρ ... Atom density / cm⁻³

I ... X-ray flux (constant)

$\frac{d\sigma}{d\Omega}$

... differential cross section

θ ... analysis angle

t ... overlayer thickness

N ... normalized XPS Intensity (peak area)

$\Lambda(E)$... electron attenuation length (from SRD 82 data base ¹)

d_s ... average separation of layers in substrate

$\Omega(E)$... acceptance solid angle of the analyzer (constant)

$A(E)$... effective substrate area (constant)

s ... mean 2D surface atom density

Indices:

s..... substrate

l..... overlayer/adlayer

The Coverage is unitless and defined by the ratio of mean 2D surface atom density of substrate to mean 2D surface atom density of overlayer. It gives the (fractional) monolayer coverage of the atomic species.

The parameters used for calculation are summarized in the following Table S1:

Table S1: Parameters for coverage and film thickness estimation via XPS

	E_{kin} / eV	$EAL / \text{Å}$		
Zr 3d _{5/2} in ZrO ₂	195	4.77	d (Pd)	2.25 Å
	1074	16.97		
Pd 3d in Pd	125	3.70	Atom density in ZrO ₂	2.98x10 ²² cm ⁻³
	919	13.07		
Pd 3d in ZrO ₂	125	3.86	Atom density in Pd	6.78x10 ²² cm ⁻³
	919	14.92		
EAL for 11 Å Pd	125	3.3		

EAL for 33 Å Pd	919	11.5		
-----------------	-----	------	--	--

B *In situ* XPS of ALD

The similar increasing of Zr coverage was confirmed by *in situ* XPS as shown Figure S1. The ZTB pressure in the NAP-apparatus was 6×10^{-6} mbar and the base pressure around 5×10^{-8} mbar; each spectrum was collected for 30 min. In the inset of the figure, the Zr 3d integrated peak area is plotted versus the exposure time. It is worth noting, that a smooth start of the Zr deposition is followed by a linear growth after about 100 s.

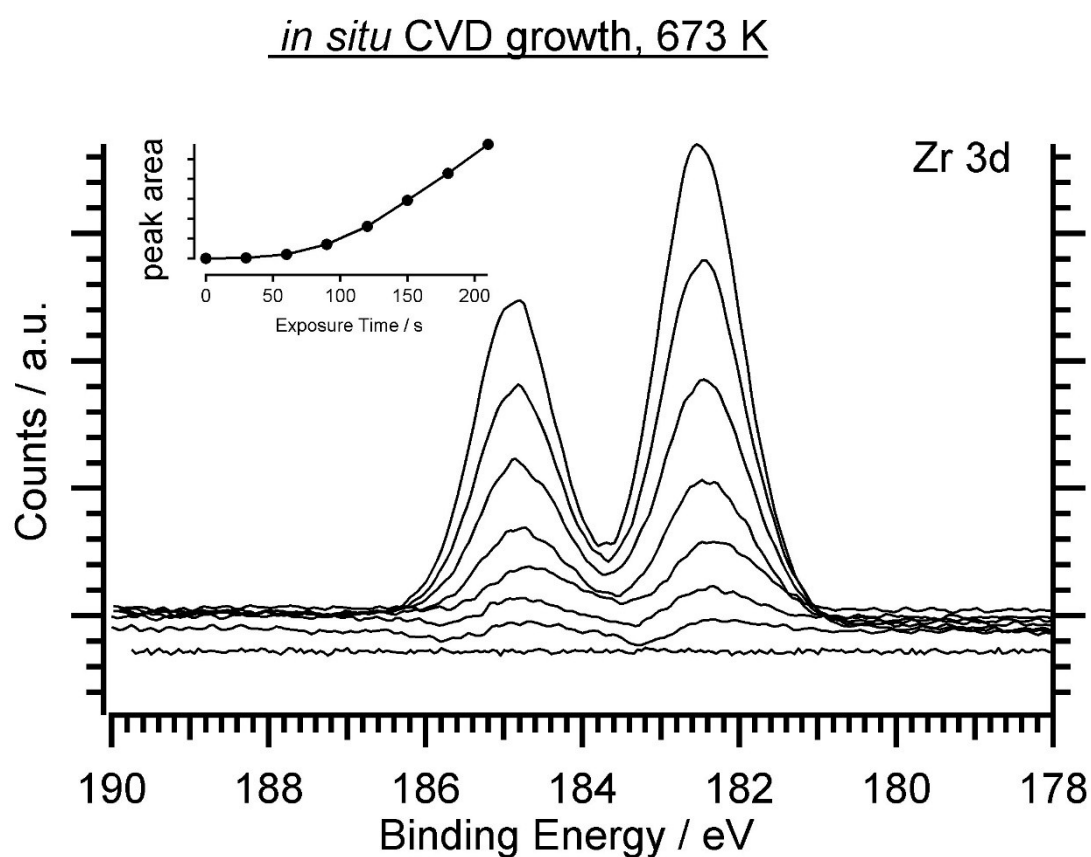


Figure S1: *In situ* CVD growth monitored at 673 K in 5×10^{-6} mbar ZTB (one spectrum each 30 sec). The inset shows the peak area evolution with exposure time.

C XPS Following Molecular Adsorption of ZTB

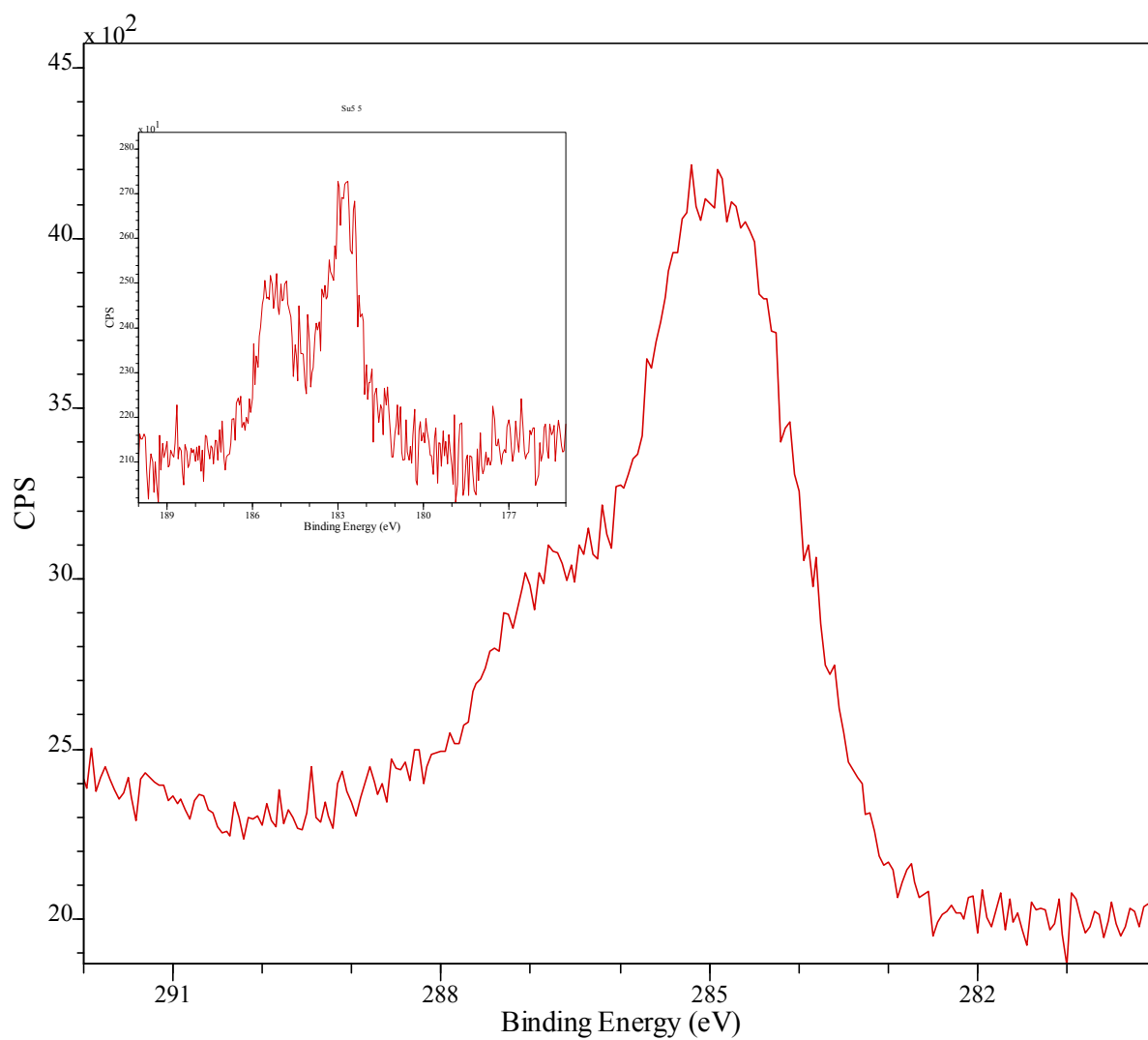


Figure S2: C 1s spectra following 2000L of ZTB exposure at 140K and subsequent heating to 273K. The inset shows the Zr 3d peak under the same conditions.

D Summary of ZTB HREELS Peak Assignments

Table S2. Major HREELS Peaks Observed from Pd(111) After Various Deposition Procedures¹

	Energy Loss (cm ⁻¹) (This work)	Vibrational Frequency (cm ⁻¹) (Literature)	Assignment
ZTB Molecular Adsorption	297 ^w	300 ²	NA
	370 ^{vw}	357 ²	NA
	483 ^w	481 ³	Zr-O vibrations
	552 ^s	550 ³	Zr-O vibrations
	780 ^{vw}	765 ⁴	$\nu(\text{C-C})$
	906 ^{vw}	924 ⁴	$\delta(\text{CH}_3)$
	1006 ^s	1027 ⁴	$\tau(\text{HCCC})$
	1192 ^w	1151 ⁴	$\delta(\text{C-C-C})$
	1238 ^{sh}	1221 & 1242 ⁴	$\nu(\text{C-C-C})$
	1372 ^{vw}	1348 & 1366 ⁴	$\delta_s(\text{CH}_3)$
	1463 ^{vw}	1449 ⁴	$\delta_{as}(\text{CH}_3) + \tau(\text{HCCC})$
	2967 ^{br}	2930-3009 ⁴	$\nu(\text{C-H}_x)$
ZTB adsorption at RT	281 ^w	300 ²	NA
	333 ^{sh}	357 ²	NA
	480 ^w	481 ³	Zr-O vibrations
	513 ^s	522 ³	Zr-O vibrations
	579 ^{vw}	550 ³	Zr-O vibrations
	752 ^s	765 ⁴	$\nu(\text{C-C})$
	854 ^s	844 ⁴	$\nu(\text{C-C})$
	925 ^s	924 ⁴	$\delta(\text{CH}_3)$

¹ Abbreviations: w, weak; s, strong; sh, shoulder; br, broad. NA: not assigned.

	1008 ^{vw}	1027 ⁴	$\tau(\text{HCCC})$
	1137 ^{vw}	1151 ⁴	$\tau(\text{HCCC})$
	1194 ^{vw}	1151 ⁴	$\delta(\text{C-C-C})$
	1322 ^{vw}	1348 & 1366 ⁴	$\delta_s(\text{CH}_3)$
	1368 ^{vw}	1348 & 1366 ⁴	$\delta_s(\text{CH}_3)$
	1443 ^w	1449 ⁴	$\delta_{\text{as}}(\text{CH}_3)+ \tau(\text{HCCC})$
	1690 ^w	1649 ⁵	$\nu(\text{C=C})$
	2949 ^{br}	2930-3009 ⁴	$\nu(\text{C-H}_x)$
ZTB adsorption on $\text{O}_{\text{ads}}/\text{Pd}(111)$ at RT	293 ^s	300 ²	NA
	345 ^{sh}	357 ²	NA
	482 ^w	481 ³	Zr-O vibrations
	546 ^w	522 ³	Zr-O vibrations
	599 ^w	550 ³	Zr-O vibrations
	771 ^w	765 ⁴	$\nu(\text{C-C})$
	914 ^{vw}	924 ⁴	$\delta(\text{CH}_3)$
	1018 ^s	1027 ⁴	$\tau(\text{HCCC})$
	1194 ^w	1151 ⁴	$\delta(\text{C-C-C})$
	1378 ^w	1348 & 1366 ⁴	$\delta_s(\text{CH}_3)$
	1459 ^w	1449 ⁴	$\delta_{\text{as}}(\text{CH}_3)+ \tau(\text{HCCC})$
	1730 ^s	1720 ⁵	$\nu(\text{R-C=O})$
	1786 ^s	1720 ⁵	$\nu(\text{R-C=O})$
	2972 ^{br}	2930-3009 ⁴	$\nu(\text{C-H}_x)$

E Decomposition of ZTB After Slight Annealing

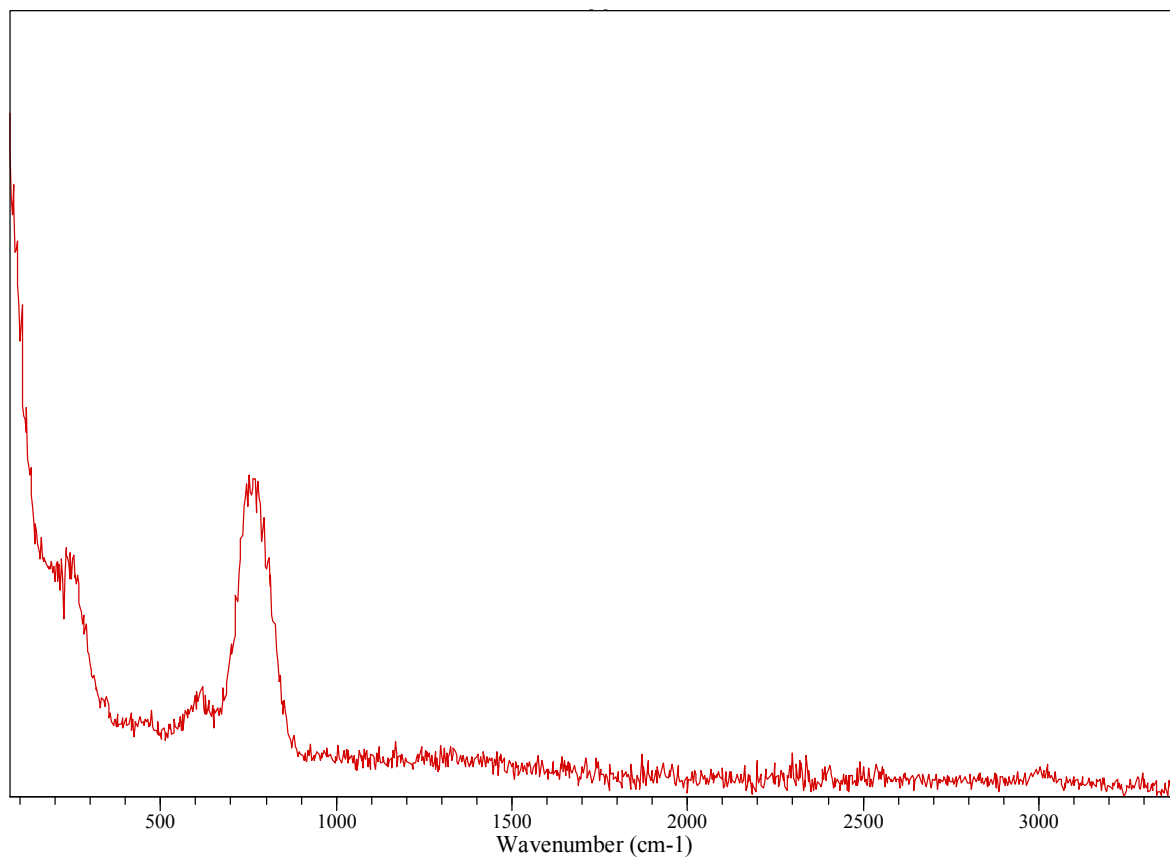


Figure S3: HREELS spectra of 2000L ZTB exposed to Pd(111) at 293K and annealed to 373K for 5 minutes.

F Catalytic Testing in Methanol steam reforming (MSR)

Both the CVD “as-prepared” (1000 L ZTB at 693 K, ~0.5 ML ZrO_xH_y) and the partially reduced samples (annealed to 700 K in 5×10^{-9} mbar vacuum after CVD) were tested in the batch reactor setup for MSR. In our standard temperature-programmed experiment up to 623 K, in both cases no positive synergistic effects toward enhanced CO_2 selectivity were observed. The well-known methanol dehydrogenation activity of clean Pd toward almost 100 % CO and H_2 was found to scale linearly with the fraction of ZrO_xH_y -free Pd surface. This is remarkable, since water-activating- and, thus, CO_2 -promoting phase boundary effects could be verified under otherwise identical MSR conditions for the related inverse Cu/ ZrO_2 and Cu/ ZrO_xH_y model catalysts⁶. Even the “hydroxylative” activation of Zr^0 on the vacuum-pre-reduced Pd/ $Zr^0/Zr^{+4}O_xH_y$ catalyst surface under MSR conditions does not promote low-temperature ($T < 623$ K) water activation and, thus, direct CO_2 -formation, which so far could be verified for the related initially bimetallic PdZn⁷, CuZn⁸ and CuZr⁶ surfaces (compare also Figure S5). Even for the later discussed intermetallic Pd-Zr bulk phase, no increase in the CO_2 formation rate could be found in MSR.

The reason for the complete absence of any CO_2 -beneficial Pd-Zr interaction was identified by *in situ* XPS measurements. In Figure S4, the evolution of the Pd 3d, Zr 3d, C 1s and O 1s regions after sequential treatment under MSR conditions, in clean methanol, water atmosphere and in O_2 are shown, starting from the CVD as-grown Pd/ ZrO_xH_y pre-catalyst state. In excess of water (water:methanol = 2:1), only very little carbon formation was observed at ~700 K (compare Figure 8, lowest panel vs. Figure S5 (different scale for C 1s)). As soon as water is switched off (giving rise to a clean methanol atmosphere), a carbon layer starts to grow. This carbon is mostly assigned to graphitic species, according to the dominant C 1s BE component at 284.2 eV and the quite low FWHM of the C 1s peak of ~0.5 eV. If the temperature is then increased in a stepwise manner, the C 1s signal gains more and more intensity. Even though graphitic carbon is known for its rather less pronounced inelastic photoelectron attenuation effect (as it

can be used as an electron transparent layer in the form of graphene), the observed large amount of carbon (well above 1 ML) must in principle cause a certain shielding effect both for the Pd 3d and Zr 3d signals if it was homogeneously covering the entire surface, especially upon consideration of the highly surface-sensitive operation mode (photoelectron kinetic energy ~ 120 eV). Surprisingly, this expectable attenuation strongly affects the Pd 3d region, but the Zr 3d signal remains almost unchanged. This effect can in principle be explained in two ways: (1) graphite only grows on Pd, but not on ZrO_xH_y , creating a thick carbon overlayer with holes at the ZrO_2 islands. Pd-Zr interface sites do not get lost but are blocked by graphitic carbon, resulting in the loss of any beneficial catalytic effect of these special sites. This hypothesis would also imply that the ZrO_2 islands are thick enough to be fully Pd 3d “attenuating”, otherwise a carbon coverage independent Pd 3d signal passing through the ZrO_xH_y islands should remain detectable. With the used photon energy of 410 eV the island height would have to exceed at least 3 ML. Considering the STM images of section 3.1.1 main paper (Figures 3 and 4), which show a ZrO_xH_y -carbon overlayer on Pd(111) with a coverage close to 1 ML after CVD, and evenly distributed clusters of Zr atoms with 1 ML height after the subsequent UHV annealing step, this scenario appears rather doubtful. Therefore, a second explanation might be more reasonable: (2) carbon grows in a “sandwich-like” fashion between Pd and ZrO_xH_y and “lifts” the ZrO_xH_y islands up. As a consequence, the Pd-Zr interfacial sites would also get lost, resulting in the discussed catalytic inactivity. Note that such tremendous amounts of carbon were found neither on clean Pd nor on clean ZrO_2 under otherwise identical conditions. Therefore, a strong enhancement of coking caused by the Pd/ ZrO_xH_y interface is strongly suggested. In such a way, the inactivity of the phase boundary in the water-containing MSR atmosphere might also be rationalized: The lift off effect might already play a role, even though the carbon formation propensity is lower due to the simultaneous water co-feed. Smaller amounts of graphitic carbon (C 1s BE = 284.3 eV) were always observed *ex situ* after MSR in the batch reactor setup. Moreover, MSR *in situ* XPS experiments at temperatures lower than

700 K are shown in Figure 9 and clearly indicate the formation of graphitic carbon also under MSR conditions. Quantification indicates a carbon coverage of 0.5-1 ML at 700 K under MSR condition (Figure S5) and around 1.5 ML at 700 K under pure methanol (Figure S4).

As the formed very thick carbon “interlayer” caused by pure methanol between 700 K and 750 K cannot be removed with H₂O and not even with O₂ at 750 K, as shown in the uppermost panels of Figure S4, its permanent poisoning effect and ineffective removal by water under MSR conditions is obvious.

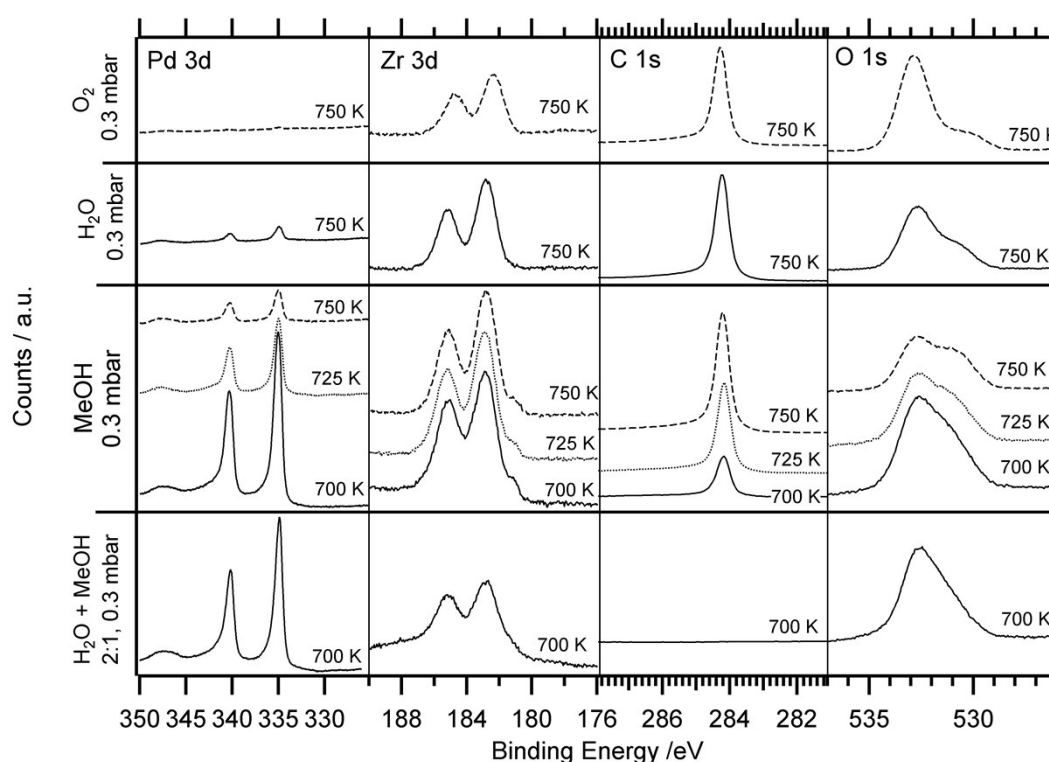


Figure S4: *In situ* NAP-XP spectra (Pd 3d, Zr 3d, C 1s and O 1s (overlapping with Pd 3p) regions) of CVD grown 0.5 ML ZrO_xH_y model catalyst (1000 L ZTB at 723 K) under water-rich MSR conditions, clean methanol, water and oxygen (details see Y-axis). No vacuum annealing treatment after CVD was performed.

Starting from a partially reduced initial state (CVD followed by vacuum annealing), Figure S5 shows the temperature-dependent evolution of the *in situ* XPS spectra under MSR conditions. Up to 423 K carbon oxygenate species can be seen at binding energies around 286-288 eV.

They arise from partial oxidation of methanol and prove the potential of the surface for methanol activation. Up to 548 K no hydroxylation is found. With increasing temperature, hydroxylation takes place under reaction conditions, along with a shift of the Zr 3d peak from 182.3 up to 183.0 eV due to reaction with H₂O in the gas feed. This indicates water activation and suggests the opening of water activation-dependent reaction channels. Moreover, graphitic carbon species (BE of 284.2 eV) are increasing between 298 and 648 K under MSR conditions. These carbon species disappear at higher temperatures. Both Pd bulk dissolution of carbon and the water gas reaction $C + H_2O \rightarrow CO + H_2$, which can cause the onset of CO formation above 650 K (see Figure 10), may be considered to explain this observation. In the O 1s region, special care has to be taken when interpreting the peak shift to higher BE as Zr hydroxylation, since also carbon oxygenates may contribute to this trend and O 1s overlaps with Pd 3p.

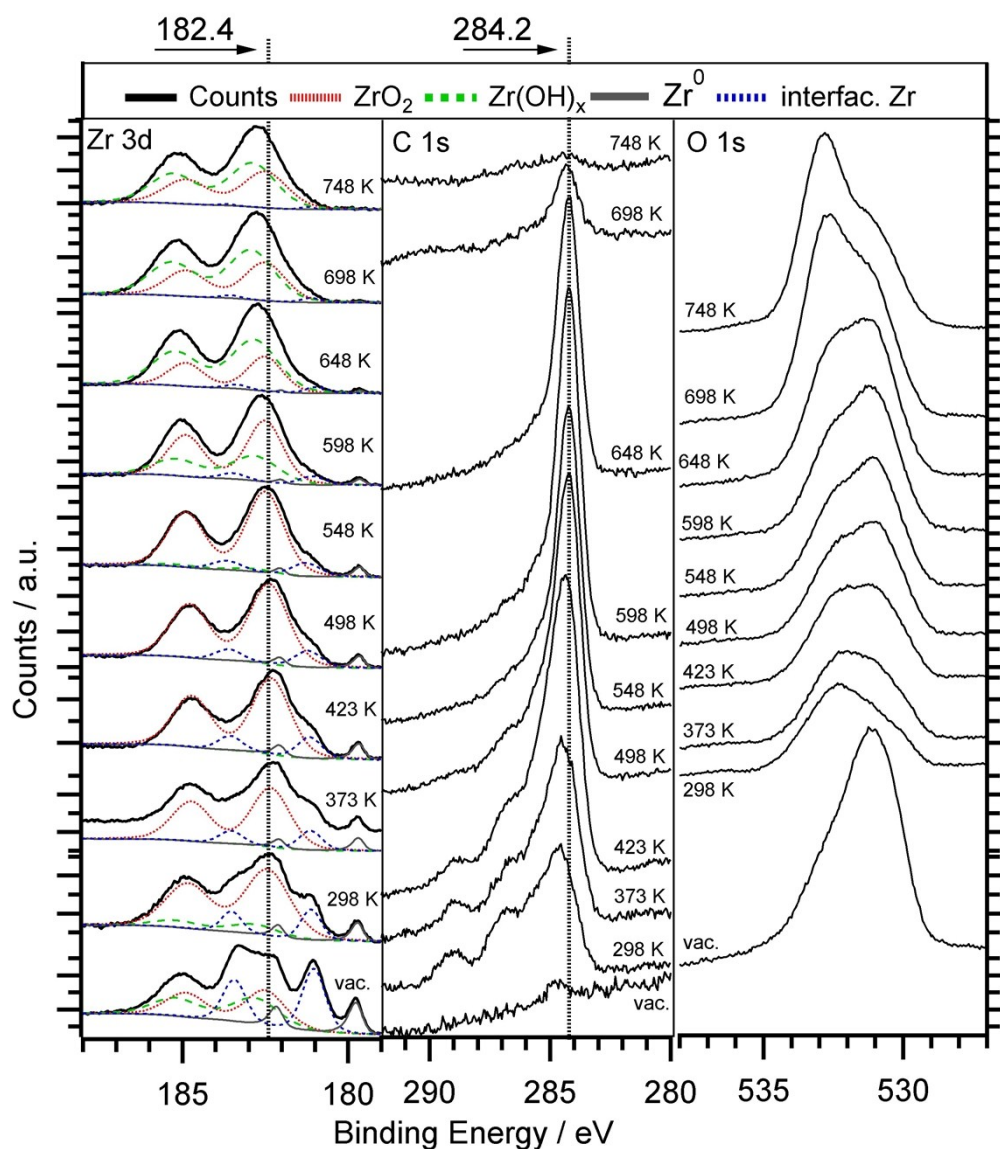


Figure S5: *In situ* NAP-XPS spectra (Zr 3d, C 1s and O 1s (overlapping with Pd 3p) regions) of 0.5 ML Zr_0/ZrO_xH_y , prepared by annealing of CVD grown ZrO_xH_y (2000 L at 723 K) in 5×10^{-8} vacuum at 700 K under water-rich MSR conditions ($H_2O:MeOH = 2:1$, $p_{total} = 0.3$ mbar).

As mentioned above, neither the CVD-as-grown $Pd/Zr^{+4}O_xH_y$ nor the mixed valence $Pd/Zr^0/ZrO_xH_y$ model catalyst (prepared by vacuum annealing of the former) showed synergistic MSR effects in the standard temperature range up to 623 K. This range represents also the accumulation- and stability region of surface carbon species, as verified by the *in situ* XPS experiments of Figure S5. As the spectra at $T > 648$ K in Figure S5 both indicate additional surface hydroxylation by water and pronounced carbon clean-off, high-temperature MSR

experiments up to 873 K were additionally performed and are shown in Figure S6. Formation of CO starts around 623 K and is assigned to the methanol dehydrogenation activity of the residual clean Pd surface. On the initially clean Pd foil (without Zr), this reaction starts also slightly above 600 K. At ~ 700 K the CO formation rate passes through a maximum, then drops steeply and even becomes negative, i.e. already formed CO is consumed, which is clearly linked to simultaneous CO_2 formation. It is rather conclusive that the CO_2 formation arises from the onset of water gas shift (WGS) activity, which is again coupled with the pronounced carbon clean-off effect starting above 650 K and shown in Figure S5. Thus, we suggest a water activation - carbon clean off - WGS scenario mediated by “de-coked” and hence, activated $\text{Pd}/\text{ZrO}_x\text{H}_y$ sites above ~ 650 K. The catalytic results of Figure S6 are therefore consistent with the *in situ* XP spectra of Figure S5. In the isothermal reaction part, CO is still formed on Pd, but partially re-consumed by the water gas shift reaction to form CO_2 . Consequently, both formation rates, CO and CO_2 , are positive. On this basis, we have to conclude that the low-temperature coking tendency, the high water-activation temperature and the CO_2 -selectivity spoiling WGS reaction on the “re-activated” catalyst limit the relevance of $\text{Pd}/\text{ZrO}_x\text{H}_y$ for selective MSR applications.

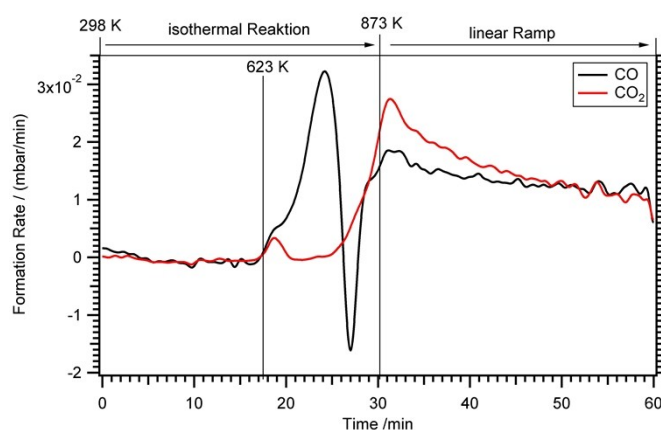


Figure S6: MSR on the CVD grown ZrO_xH_y model catalyst under water-rich MSR conditions (water:methanol = 2:1, $p_{\text{total}} = 36$ mbar). The exposure was about 1000 L ZTB at 700 K and the

initial coverage with Zr estimated to ~ 0.4 ML. The temperature range of the MSR experiment was extended to 873 K.

G Depth Profiling XPS of a pre-oxidized Zr foil after DRM

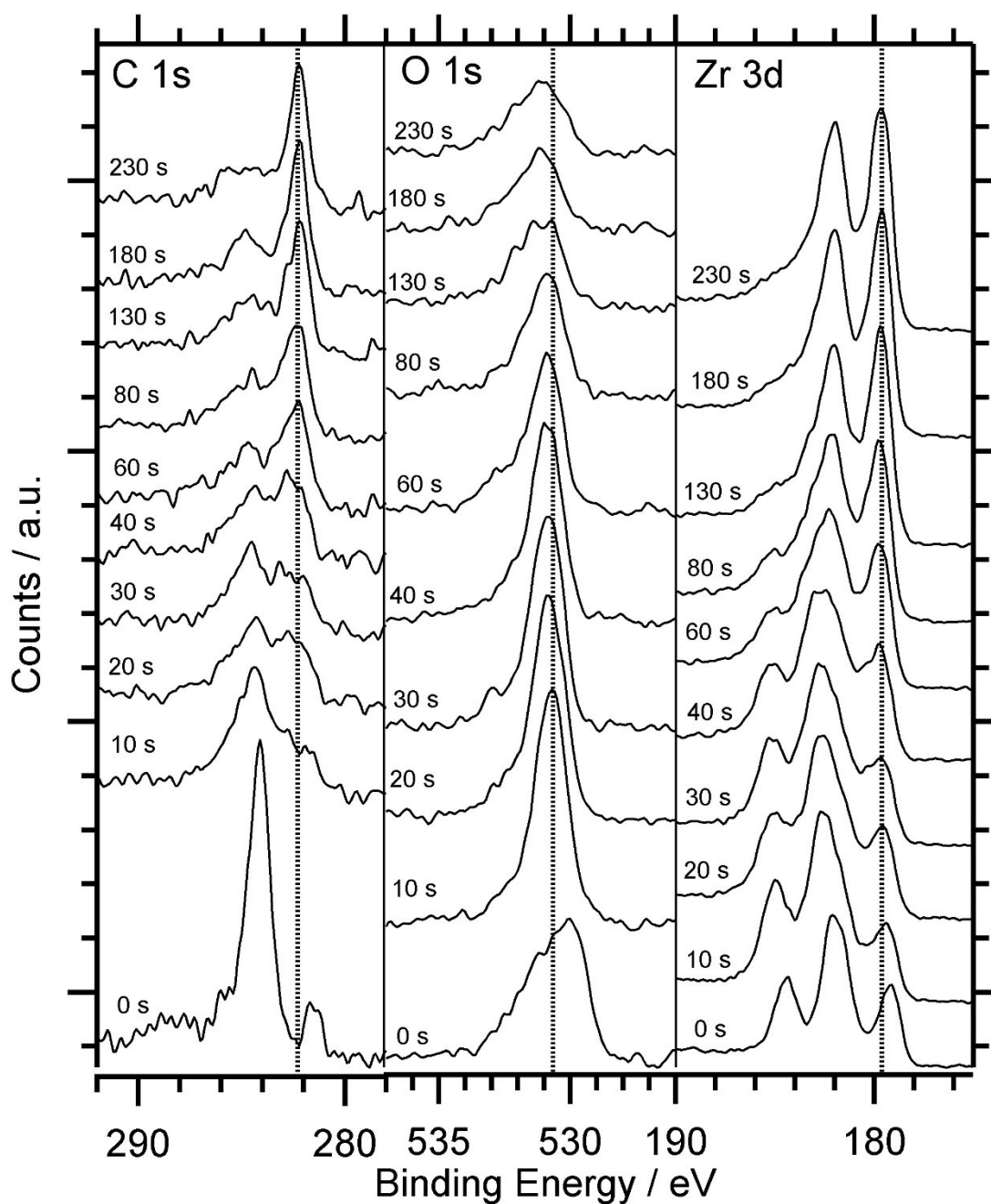


Figure S7: Destructive depth profiling of pre-oxidized Zr foil after DRM with Ar^+ sputtering.

The sputter time is labeled in the figure. 10 s of sputter time correspond to approximately 1 nm.

In the DRM experiment, ZrO_2 gets fully reduced (see Figure 12 main paper). With this reduction, the formation of a zirconium carbide comes along, indicated by a binding energy of C 1s at 282.0 eV beside a hydrocarbon peak at 284.5 eV. Zr 3d Binding Energy was found at 179.4 eV for the surface zirconium carbide and 182.4 eV for the surface oxidation due to the transport via air. Destructive depth profiling of the sample after methane dry reforming (spectra shown in Figure 12) clearly indicates that the hydrocarbon overlayer is very thin (~ 5 nm) and the Zr carbide reaches much deeper (>20 nm). Due to the transport over air a thin (< 5 nm) passivating ZrO_2 overlayer (Zr 3d BE 182.4 eV) is formed and cannot be seen after DRM when sample was not exposed to air (compare Figure 13). With removal of this oxide layer and the carbon species at 284.0 eV that are formed under DRM and increase in quantity due to air exposure by Ar^+ sputtering, metallic Zr and a carbon peak at 282.0-282.1 eV arises. This near-surface carbon species is also seen in XPS right after DRM (Figure 13) and assigned to the formation of Zirconium carbide⁹. Summing up, the sample can be described as a layered system consisting of Zr (substrate), $\text{ZrC}(>20$ nm) and on top $\text{ZrO}_2/\text{C}_x\text{H}_y$ (~ 5 nm).

H XRD Analysis of the nominal 2:1 Pd-Zr intermetallic compound before and after DRM

For the DRM-active intermetallic Pd-Zr bulk phase catalyst, XRD patterns before and after the reaction were collected in analogy to the highly MSR-active Cu-Zr catalyst. For Cu-Zr, a straightforward assignment of the pattern to a single intermetallic Cu-Zr phase in contact to metallic Cu was possible. In contrast, for the Pd-Zr intermetallic phase, this was not an easy task, because the melt-prepared sample is much less homogeneous. A number of possible intermetallic compounds in varying stoichiometries (in accordance with the overall 2:1 stoichiometry of Pd:Zr in the initial melt) potentially match the pattern recorded prior to DRM, including Pd_3Zr and Pd_4Zr_3 .¹⁰ The presence of Pd_2Zr can be ruled out due to mismatch with

reference diffractograms. A small amount of oxidized monoclinic ZrO_2 can also be found. After DRM, tremendous changes in the diffraction pattern indicate massive structural changes, alongside a further increase in sample inhomogeneity. Pd_3Zr is not present anymore, but a number of new intermetallic/oxo-intermetallic compounds have been formed, including Pd_9Zr and Pd_4Zr_3 . A small amount of monoclinic and tetragonal ZrO_2 is also present, most probably stemming from partial oxidative decomposition of the Pd-Zr intermetallic compounds. Generally, it seems plausible, that the Pd-Zr phases are not as much affected by selective oxidative decomposition under DRM conditions as it was the case for Cu-Zr under MSR conditions, because the DRM reaction conditions are far more reducing. For pure ZrO_2 on Zr, complete reduction of ZrO_2 and the formation of ZrC was found after DRM at 1073 K. In the post-DRM XRD pattern, metallic Zr could be found.¹¹ Note that due the fact the Pd-Zr intermetallic phase has been prepared on a Ta crucible, the not assigned peaks in Figure S5 arise from metallic Ta or Ta_2O_5 . However, no Ta-Pd or Ta-Zr phases could be identified, indicating that metal intermixing during the preparation process is absent.

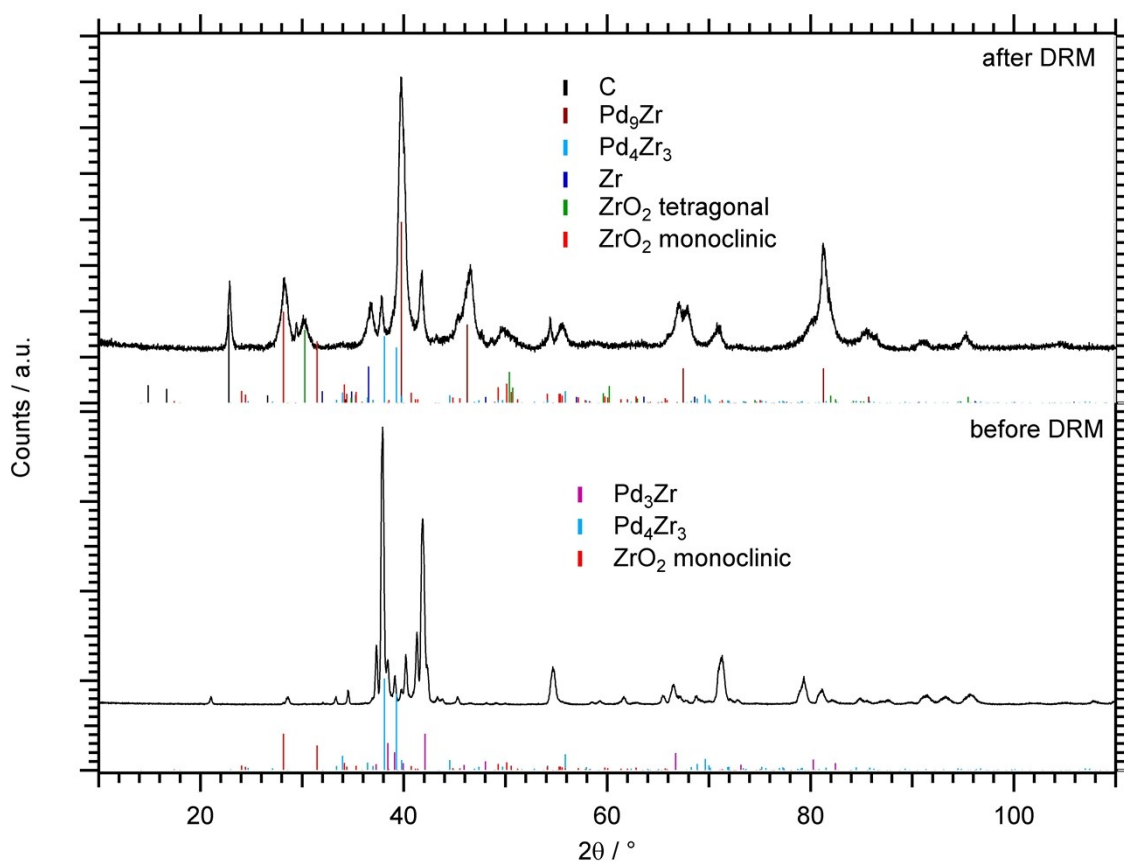


Figure S8: X-ray diffraction patterns of the Pd-Zr bulk sample (nominal composition 2:1 = Pd-Zr). The bars indicate the reference peaks of the present phases.

I References

1. C. J. Powell and A. Jablonski, *NIST Electron Effective-Absorption-Length Database SRD 82*. National Institute of Standards and Technology: Gaithersburg, 2011; Vol. Version 1.3.
2. C. T. Lynch, K. S. Mazdiyasi, W. J. Crawford and J. S. Smith, *Anal. Chem.*, 1964, **36**, 2332-&.
3. R. Verhoef, P. Raynaud, S. Ligot, R. Snyders, T. Nelis, R. V. Gonzalez and S. Vitale, 21st International Symposium on Plasma Chemistry, 2013; p OR 214.
4. Y. Sert, L. M. Singer, M. Findlater, H. Dogan and G. Cirak, *Spectrochim. Acta A*, 2014, **128**, 46-53.

5. H. J. Oelichmann, D. Bougeard and B. Schrader, *J. Mol. Struct.*, 1981, **77**, 179-194.
6. L. Mayr, B. Klötzer, D. Zemlyanov and S. Penner, *J. Catal.*, 2015, **321**, 123-132.
7. C. Rameshan, W. Stadlmayr, S. Penner, H. Lorenz, N. Memmel, M. Hävecker, R. Blume, D. Teschner, T. Rocha, D. Zemlyanov, A. Knop-Gericke, R. Schlögl and B. Klötzer, *Angew. Chemie*, 2012, **124**, 3057-3061
8. C. Rameshan, W. Stadlmayr, C. Weilach, S. Penner, H. Lorenz, M. Hävecker, R. Blume, T. Rocha, D. Teschner, A. Knop-Gericke, R. Schlögl, N. Memmel, D. Zemlyanov, G. Rupprechter and B. Klötzer, *Angew. Chem., Int. Ed.*, 2010, **49**, 3224-3227
9. R. Kaufmann, H. Klewe-Nebenius, H. Moers, G. Pfennig, H. Jenett and H. J. Ache, *Surf. Interface Anal.*, 1988, **11**, 502-509.
10. L. A. Bendersky, J. K. Stalick and R. M. Waterstrat, *J. Alloys Compds.*, 1993, **201**, 121-126
11. M. Eshed, S. Pol, A. Gedanken, M. Balasubramanian, *Beilstein J. Nanotechnol.*, 2011, **2**, 198-203